Supplementary Information for

A Fabrication Strategy for Millimeter-Scale, Self-Sensing Soft-Rigid Hybrid Robots

Hun Chan Lee[1], Nash Elder[1], Matthew Leal[2], Sarah Stantial[1],
Elenis Vergara Martinez[3], Sneha Jos[4], Hyunje Cho[1],
Sheila Russo[1*]

[1*]Department of Mechanical Engineering, Boston University, 110
Cummington Mall, Boston, 02215, MA, USA.
[2]Department of Biomedical Engineering, Boston University, 44
Cummington Mall, Boston, 02215, MA, USA.
[3]Department of Biomedical Engineering, Florida International
University, 10555 W Flagler St, Miami, 33174, FL, USA.
[4]Department of Physics, Boston University, 590 Commonwealth Ave,
Boston, 02215, MA, USA.

*Corresponding author(s). E-mail(s): russos@bu.edu;
Contributing authors: hclee94@bu.edu; njelder@bu.edu; mpl@bu.edu;
sats23@bu.edu; elenismilenys@outlook.com; sjos@bu.edu; cho95@bu.edu;

The PDF file includes:

- Supplementary Text
- Supplementary Figs. 1 to 12
- Supplementary Tables 1 to 4
- Legends for Supplementary Movies 1 to 8
- SI References

Other supplementary materials for this manuscript include the following:

- Supplementary Movies 1 to 8

Supplementary Text

Geometric Modeling for Translational SHY Robotic Module

The range of motion of the translational SHY robotic module is mainly affected by the maximum folding angles of flexible joints from the Sarrus linkages. As illustrated in Supplementary Fig. 1a, the maximum bending angle of the flexible joints depends on the thickness of the structural layers (t) and the gap between two structural components (g)[13, 17]. Applying Supplementary Equation (1), the maximum bending angle (θ) of the flexible joints in degrees can be calculated:

$$\theta = 180 - 2\tan^{-1}\left(\frac{2t}{g}\right) \tag{1}$$

This bending angle can be used to define maximum translation in the z-direction of a translational actuator (Supplementary Fig. 1b) as described in Supplementary Equation (2):

$$h_T = 2Csin(\theta) \tag{2}$$

where C is the chord length of circular Sarrus linkages, and h_T is the translated distance.

Geometric Modeling for Bending SHY Robotic Module

The bending SHY robotic module consists of a constraint joint and Sarrus linkage arms (Supplementary Fig. 1c). The embedded PTFE soft-foldable actuator moves along an arc centered at the constraint. Like other flexible joints, the maximum bending angle (θ_b) of this constraint joint can be calculated using Supplementary Equation (1). Additionally, the maximum bending angle of the bending SHY robotic module can be constrained by the chord length of the arms. Given the distance between the centers of top and bottom surfaces (d), the distance between the bending joint and the center (r), and the fixed gap between the top and bottom structural layers (k), θ_b can be derived:

$$\theta_b = cos^{-1}(\frac{r^2 + \sqrt{r^2 + k^2} - d^2}{2r\sqrt{r^2 + k^2}}) - (90 - tan^{-1}(\frac{r}{k})) \tag{3}$$

As described in Supplementary Equation (3), shorter chord lengths of arms would result in a smaller maximum bending angle by mechanically stopping the actuator from further bending.

Geometric Modeling for roto-translational SHY robotic module

The roto-translational SHY robotic module can make interdependent, roto-translational movement by connecting the top and bottom sides of the system with circular-shaped arms. The bottom side of the embedded soft-foldable actuator is not constrained such that it can freely rotate about the center axis. Thus, as the actuator expands, the arms bend about the flexible joints and cause the top side of the module to rotate with respect to the bottom side (Supplementary Fig. 1d).

The rotation that occurs during the extension can be found using the kinematics of the mechanical controller shown in Supplementary Fig. 1d. The constraining arm that causes the rotating motion has a constant chord length C_0. The radius of the actuator (r), the initial arc angle between two flexible joints of an arm (ϕ_0), and the fixed gap between the top and bottom sides of the actuator (k) are also known (Supplementary Fig. 1e). Given C_0 and k, the fixed distance from the bottom to the top side of the roto-translational SHY robotic module, C_i, can be computed:

$$C_i = \sqrt{C_0^2 + k^2} \tag{4}$$

Using the given parameters, a variable chord length (X_n) can be calculated as in Supplementary Equation (6).

$$\begin{aligned} C_i^2 &= X_n^2 + (k + h_R)^2 && (5)\\ X_n &= \sqrt{C_0^2 - 2kh_R - h_R^2} && (6) \end{aligned}$$

Then, the variable arc angle (ϕ_n) resulting from the variable chord length (X_n) can be calculated in Supplementary Equation (7).

$$X_n = 2rsin(\frac{\phi_n}{2}) \tag{7}$$

Finally, The resulting rotational motion, ϕ_r, can be calculated by subtracting ϕ_n from ϕ_0.

$$\phi_r = \phi_0 - \phi_n \tag{8}$$

Output Torque of Roto-translational SHY Robotic Module

The output torque of the roto-translational SHY robotic module can be calculated by using the geometric translation-rotation relationship with output force data. This relationship can be derived using the principle of virtual work. Under the principle of virtual work, the work done by external forces (dW_{Ext}) should be equal to the work done by internal forces (dW_{In}). Using this, Supplementary Equation (10) can be derived,

$$\begin{aligned} dW_{Ext} &= dW_{In} && (9)\\ Td\phi + Fdh &= Pd\forall && (10) \end{aligned}$$

where T is the output torque, ϕ is the rotation angle of the actuator, h is the height of the actuator, P is the internal pressure and $\forall$ is the internal volume. To compute the maximum output torque of the roto-translational SHY robotic module, we assumed that it purely exerts torque. In addition, we assumed that when the output force of the roto-translational SHY robotic module was measured, the actuator was purely exerting force. With those assumptions, Supplementary Equation (12) can be derived.

$$\begin{aligned} Td\phi &= Fdh && (11)\\ T &= Fdh/d\phi && (12) \end{aligned}$$

Peeling Test

Polytetrafluoroethylene (PTFE) films are well-known for their non-stick properties, which are a result of the stable bonding between carbon and fluorine atoms, providing hydrophobic and chemical resistance characteristics. However, untreated PTFE films do not readily bond with acrylic adhesive films, requiring either a wet or dry surface treatment process to promote adhesion. In this paper, a dry etching process known as plasma etching is performed to modify the chemical properties of PTFE films to build soft-foldable actuators. As indicated in [1, 4, 15], H_2 gas is an effective process gas to promote defluorination of PTFE surfaces. In addition to the processing gas, the level of defluorination heavily depends on etching power and time [5, 7] as well.

A supported T-peel test (ASTM D1876 standard) was conducted using a tensile testing machine (5943, Instron) to measure the peel strength of 25 μm PTFE films (McMaster Carr Supply Company) bonded with an acrylic adhesive film (FR1500, DuPont de Nemours, Inc.) and determine the ideal plasma etching recipe. The PTFE and acrylic adhesive films were cut in the dimensions of 25 mm width and 100 mm length. The PTFE was then plasma etched using H_2 gas at various power settings from 50 W to 450 W, which is the maximum power of the reactive ion etcher (790, Plasma-Therm), with increments of 50 W. The etching time was kept at a constant 5 min. The samples were then prepared by bonding two sheets of PTFE films and an acrylic adhesive film using a heat press at 200 °C and 350 kPa.

The results of the peel strength are shown in Supplementary Fig. 5 and Supplementary Table 2. For each sample, the T-peel force was determined by removing the top and bottom 10 % of data and calculating the average. This is done to avoid consideration of the ramp-up and failure into the average. As indicated in Supplementary Fig. 5, peel strength increases as the plasma etching power increases, resulting in the sample that was plasma etched at 450 W for 5 min to have the highest force required to peel.

Fatigue Test

The durability of the proposed SHY robots was assessed by inflating and deflating the embedded PTFE soft-foldable actuators 500 times and measuring the changes in the pressure-volume curve over the cycles. As the results indicate, none of the modules broke during the test. However, changes in the pressure-volume curve were observed over the cycle. As shown in Supplementary Fig. 8, more working fluid was injected into the actuators to reach the desired pressure as the number of cycles increased. Similar to other soft robots[9, 11, 12], this is likely to happen because of the stretch of elastic films caused by the relaxation of polymer chains. Additionally, hysteretic behavior from the pressure-volume curves was noted. This likely happened due to the stretch of soft, flexible materials and the slower retraction of the injected fluid. The slower retraction speed would be caused by the small diameter of the microfluidic tubing (i.e., 305 μm). The small diameter of the microfluidic tubing likely caused an increase in the flow resistance for both injection and retraction of the working fluid. This increase in the flow resistance is more notable during retraction because, during this phase, the PTFE layer starts to close off the inlet hole as the internal pressure of the balloon drops.

Sensor Modeling and Characterization

The modeling of ionic resistive sensors is based on Pouillet's law, $R = \rho L_{eff}/A$, which assumes a resistance depends on a cross-sectional area A and length L_{eff}, and resistivity ρ of a resistor. However, unlike conventional resistors which have a constant cross-sectional area, the proposed ionic resistive sensor has a variable cross-sectional area. This variable cross-sectional area can be calculated as $A = \pi(Kr)^2$ where r is the electrode plate radius and K is a corrective multiplicative function that takes account of the irregular geometry of the PTFE soft-foldable actuator. The term acts as a multiplicative function K on the electrode radius by increasing linearly as the actuator expands. Each type of SHY robotic module has a different corrective factor due to the various constraints and differences in geometry between modules.

$$K_{translation} = \{x : \exists\ h_T \in s.t.\ x = 0.9 + 0.1h_T\ and\ x \in [1.55, 2]\} \tag{13}$$

$$K_{bending} = \{x : \exists\ h_B \in s.t.\ x = 0.7 + 0.1h_B\ and\ x \in [1.35, 1.9]\} \tag{14}$$

$$K_{roto-translation} = \{x : \exists\ h_R \in s.t.\ x = 1.55 + 0.1h_R\ and\ x \in [1.4, 1.9]\} \tag{15}$$

For the translational case, it is assumed that the actuator geometry is a cylinder with a variable cross-sectional area, and resistance increases with respect to the height of the actuator (h_T). The bending case operates under the same assumptions but changes its resistance along an arc length (h_B). The length assumed for this cylinder follows an arc length calculation of $h_B = r\theta_b$. The roto-translational case operates similarly to the translation actuator, resulting in the change in resistance with respect to the height of the actuator (h_R).

The sensor can be characterized by measuring the resistance across the embedded electrodes at various expanded states. When placed in a voltage-dividing circuit (Supplementary Fig. 9), the change in resistance will change the voltage output across a shunt resistor, as described in Supplementary Equation (16).

$$V_{shunt} = V_{in}\frac{R_{shunt}}{R_{shunt} + R_{sensor}} \tag{16}$$

This voltage output can then be related to the physical inputs of the SHY robotic module. As a result, this relation can be applied to track linear extension, bending angle, and both extension and rotation in the translational, bending, and roto-translational SHY robotic modules.

Optimization of Input Frequency

An ionic resistive sensor requires an alternating current (AC) stimulating signal with an optimal operating frequency for accurate and consistent measurements. There is a trade-off between selecting a slow input frequency (<1 kHz) and a high input frequency (>10 kHz). With a slow input frequency, ions would be polarized and reduce conductivity. Likewise, AC signals with high operating frequency would cause ions to move within the solution rather than oscillate across electrodes. Thus, the choice of input frequency is crucial to balance the conductance of the sensor and minimize the effects of ion polarization.

In this work, the optimal operating frequency for the proposed ionic resistive sensor was determined experimentally. To perform the experiment, a translational actuator with an integrated ionic resistive sensor was connected to a voltage-dividing circuit (Supplementary Fig. 9). Different input frequencies were applied to the circuit, and the resulting change in voltage across the shunt resistor of the voltage-dividing circuit was measured using a true RMS-DC sensor (LTC1968, Analog Devices Inc.). As shown in Fig. 5b, the result indicates that an AC signal with a frequency of 10 kHz provided the largest and most consistent change in voltage as the actuator moved through its range of motion. This frequency was selected as the optimal operating frequency for the ionic resistive sensor in this particular setup.

Capacitive Effect Measurement Test

At small distances, the electrodes could theoretically operate as a parallel plate capacitor, resulting in the formation of a parallel resistive-capacitive (RC) sensor. To account for this, the significance of capacitive effects was explored. As Supplementary Equation (17) indicates, when the resistance of the sensor (R) and input frequency (f) are fixed, a small phase shift would indicate a low magnitude of capacitance.

$$\phi_{RC} = tan^{-1}(-R2\pi fC) \tag{17}$$

A testing setup was created by placing a translational sensing module in the voltage-dividing circuit and providing a 10 kHz input frequency. The phase shift between the input and output signal from the sensor was measured using a digital oscilloscope (2567, B&K Precision). From this experiment, it was determined that the phase shift is always less than 10°, indicating the capacitive effect is negligible.

Scalability

We demonstrated the scalability of our SHY manufacturing method by fabricating the SHY robotic modules at a 5 mm OD (Supplementary Fig. 2a-c). Similar to an 11.5 mm OD SHY robotic module, a 5 mm OD SHY robotic module comprises a 3 mm OD soft-foldable actuator, an ionic resistive sensor, and a mechanical controller.

Supplementary Figs. 2d-i illustrate the mechanical characterizations of the scaled-down version of the SHY robotic modules. We performed the same mechanical performance characterization experiments on each type of the scaled-down SHY robotic modules as performed on their scaled-up counterparts. As shown in Supplementary Figs. 2d-f, each module was pressurized up to 140 kPa to characterize its range of motion. A 5 mm OD translational module can extend up to 2.2 mm ± 0.07 mm (Supplementary Fig. 2d), a 5 mm OD bending module can bend up to 45° ± 0.9 ° (Supplementary Fig. 2e), and a 5 mm OD roto-translational module can extend up to 2.41 mm ± 0.1 mm and simultaneously rotate 40° ± 1.67 ° (Supplementary Fig. 2f).

Similarly, output force and torque performance were characterized (Supplementary Figs. 2g-i) by pressurizing each module up to 180 kPa at 0% expansion state. The results indicate that the 5 mm OD translational, bending, and roto-translational modules can generate up to 777 mN ± 7 mN (Supplementary Fig. 2g), 480 mN ± 14 mN (Supplementary Fig. 2h), and 723 mN ± 6.5 mN (Supplementary Fig. 2i), respectively.

Additionally, the roto-translational module can exert 6.2 Nmm ± 41 mNmm of torque. The output forces and torque generated by the miniature SHY robots were observed to be similar to the values predicted by the theoretical model. At the maximum input pressure, the error between the model and the actual response of the translational, bending, and roto-translational modules was 8.3 %, 0.8 %, and 5.4 %, respectively. The maximum output forces indicate that the miniature SHY robots hold promise for use in surgical procedures involving delicate tissues. For instance, vascular surgery and neurosurgery often necessitate average forces ranging from 100 to 200 mN for tissue penetration [3].

Supplementary Figs. 2j-l depict the sensor characterization plots, illustrating the normalized voltage (V/V_0) plotted against the range of motion of each actuator. In the scaled-down SHY robotic modules, the 680 kΩ shunt resistor of the voltage divider from Supplementary Fig. 9 was replaced with a 470 kΩ resistor. This substitution was made because a smaller size would lead to a smaller resistance, as predicted by Pouillet's law. Supplementary Fig. 2j shows the normalized voltage (V/V_0) across the sensor versus the extension for the translational SHY robotic module. The sensor maps across the entire range from 0 to 2.2 mm range of linear extension. Supplementary Fig. 2k shows the normalized voltage across the sensor versus the bending angle for the bending SHY robotic module. The sensor maps across the entire 0 to 45° range of bending. Finally, Supplementary Fig. 2l shows the sensor characterization of the roto-translational SHY robotic module, which maps across the full deflection range of 0 to 2.4 mm of extension. The max standard deviation was found to be 0.004 for the translational actuator, 0.006 for the bending actuator, and 0.013 for the roto-translational actuator. Similar to their larger counterpart, the scaled-down SHY robotic module sensors also demonstrate a nonlinear, monotonic response and could be employed for sensor feedback in robot position control as well.

SHY Continuum Robot Modeling

The tip position of the SHY continuum robot can be defined using homogeneous transformation matrices. The translational SHY robotic module is designed to extend linearly with a stabilizing arm structure to promote its movement in the local z-axis only, which is defined to run along the direction the module extends with the origin at the center of the module on the bottom plate. The transformation can be represented as a prismatic joint with translation in the z-axis, with no rotation out of the plane. The rotation matrix R_T is an identity matrix represented in Supplementary Equation (18) since there is no rotation in this joint.

$$R_T = \begin{bmatrix} 1 & 0 & 0 \\ 0 & 1 & 0 \\ 0 & 0 & 1 \end{bmatrix} \tag{18}$$

The translation is represented by the vector p_T in Supplementary Equation (19). The term h_T is the term tracking the length of the translational module, which is extended linearly.

$$p_T = \begin{bmatrix} 0 \\ 0 \\ h_T \end{bmatrix} \tag{19}$$

The motion of the bending SHY robotic module can be described as a rotation about an axis with translation along a plane. The bending module is oriented such that the rotation caused is about the x or y axis. The transformations are described as rotation matrices about the x or y axis, with translation in two directions. Supplementary Equation (20) represents the rotation about the x axis, and Supplementary Equation (21) represents the translation along the $y-z$ plane for one module orientation:

$$R_{B_x} = \begin{bmatrix} 1 & 0 & 0 \\ 0 & cos\theta_b & -sin\theta_b \\ 0 & sin\theta_b & cos\theta_b \end{bmatrix} \tag{20}$$

$$p_{B_x} = \begin{bmatrix} 0 \\ -L_{b1} \\ L_{b2} \end{bmatrix} \tag{21}$$

Using geometry, L_{b1} and L_{b2} can be defined as shown in Supplementary Equation (22) and Supplementary Equation (23),

$$L_{b1} = r - rcos(\theta_b) \tag{22}$$

$$L_{b2} = rsin(\theta_b) \tag{23}$$

where r is the distance between the bending joint and the center of the actuator, and θ_b is the bending angle. Similarly, Supplementary Equation (24) represents the rotation about the y axis, and Supplementary Equation (25) represents the translation along the $x-z$ plane for one module orientation.

$$R_{B_y} = \begin{bmatrix} cos\theta_b & 0 & sin\theta_b \\ 0 & 1 & 0 \\ -sin\theta_b & 0 & cos\theta_b \end{bmatrix} \tag{24}$$

$$p_{B_y} = \begin{bmatrix} -L_{b1} \\ 0 \\ L_{b2} \end{bmatrix} \tag{25}$$

The roto-translational SHY robotic module can be modeled as follows. The distance that the actuator has extended (h_R) can be used for the translation component of the actuator. This transformation consists of a rotation about and translation along the z axis. This can be represented as a prismatic and revolute joint. Rotation about the z axis is represented in Supplementary Equation (26) and the translation by Supplementary Equation (27).

$$R_R = \begin{bmatrix} cos\phi_r & -sin\phi_r & 0 \\ sin\phi_r & cos\phi_r & 0 \\ 0 & 0 & 1 \end{bmatrix} \tag{26}$$

$$p_R = \begin{bmatrix} 0 \\ 0 \\ h_R \end{bmatrix} \tag{27}$$

The position and orientation of each module are used to fill the homogeneous transformation matrix, represented by the matrix in $SE(3)$ in Supplementary Equation (28).

$$T = \begin{bmatrix} R & p \\ 0 & 1 \end{bmatrix} \tag{28}$$

In the SHY continuum robot, the pose of each module is influenced by the preceding modules, similar to how the joints of a rigid robotic arm depend on the previous joint movements. By knowing the transformation of each module, which can be obtained from the voltage readouts of the integrated ionic resistive sensors, the position of the robot's tip can be determined using forward kinematics. A fixed base frame is established at the base of the SHY continuum robot, where the robot is tethered. The forward kinematics from this base frame to the tip of the robot can be calculated. The forward kinematics to compute the tip position for a three-module configuration is shown in Supplementary Equation (30), where terms T_1, T_2, and T_3 represent the transformations of embedded modules, and T_{sp} represents a spacer placed in between modules that accounts for the gap (h_g) placed in the fabrication of the SHY continuum robot.

$$T_{sp} = \begin{bmatrix} 1 & 0 & 0 & 0 \\ 0 & 1 & 0 & 0 \\ 0 & 0 & 1 & h_g \\ 0 & 0 & 0 & 1 \end{bmatrix} \tag{29}$$

$$T_{tip} = T_1 \cdot T_{sp} \cdot T_2 \cdot T_{sp} \cdot T_3 \tag{30}$$

Batch Fabrication

Our approach enables the simultaneous production of multiple SHY robotic modules within a single laminate. Supplementary Fig. 12 illustrates a 5×5 cm square laminate containing 15 miniature (5 mm) SHY robotic modules. The diode-pumped solid-state (DPSS) ultraviolet (UV) laser precision micromachining system (Coherent Matrix 355nm, 5W) used in this study has a working area of 15× 15cm. Thus, up to ≈105 scaled-down (5 mm OD) SHY robotic modules can be manufactured in a single batch, if desired. Additionally, this setup enables the simultaneous fabrication of various types and sizes of SHY robotic modules, facilitating the construction of the SHY continuum robot and reducing overall fabrication time.

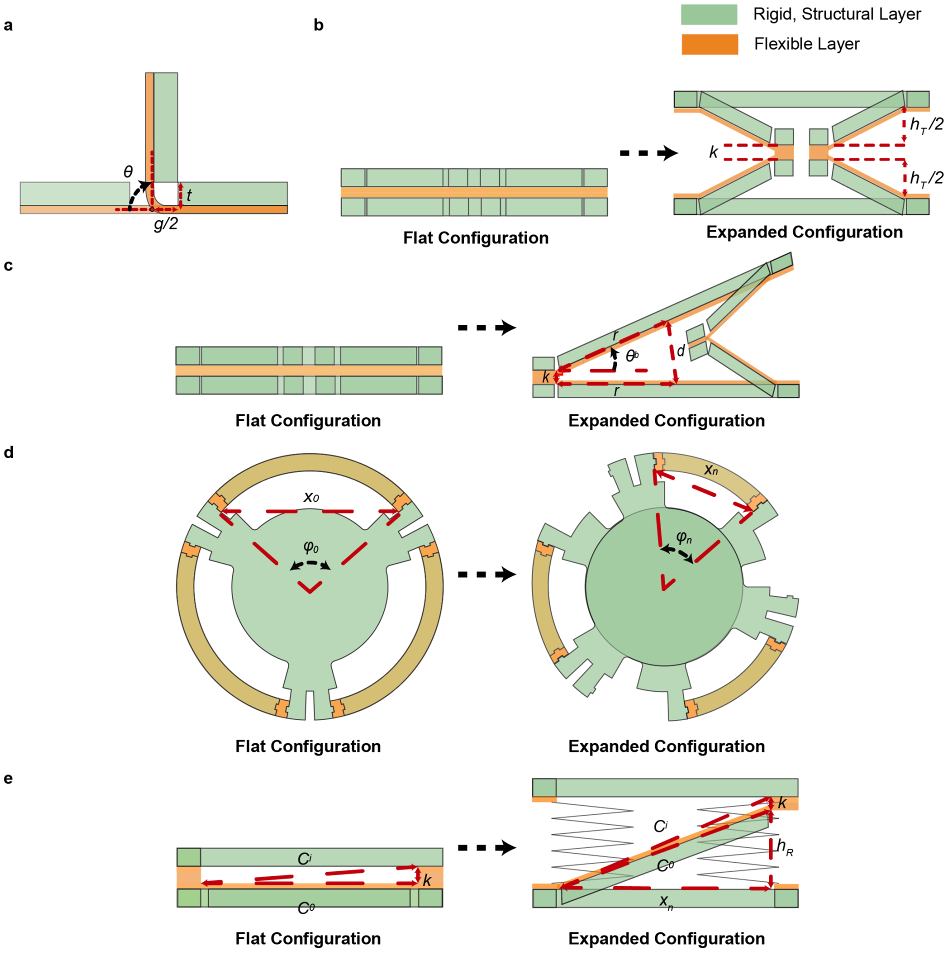

Fig. 1 **Schematics for SHY robotic module kinematics**. (a) The bending angle, θ, depends on the thickness, t, and the gap, g, between two rigid materials. (b) Flat and expanded configuration of the translational SHY robotic module. The extension depends on the bending angle of Sarrus linkages and the chord length of Sarrus linkages. (c) Flat and expanded configuration of the bending SHY robotic module. The bending angle depends both on the bending angle of the constraining joint and the chord lengths of the Sarrus linkages. (d) Top view of the roto-translational SHY robotic module. As the module expands, the system performs roto-translation, resulting in a smaller ϕ_n. The difference between ϕ_0 and ϕ_n is the rotation of the system. (e) Flat and expanded configuration of the roto-translational SHY robotic module in side view.

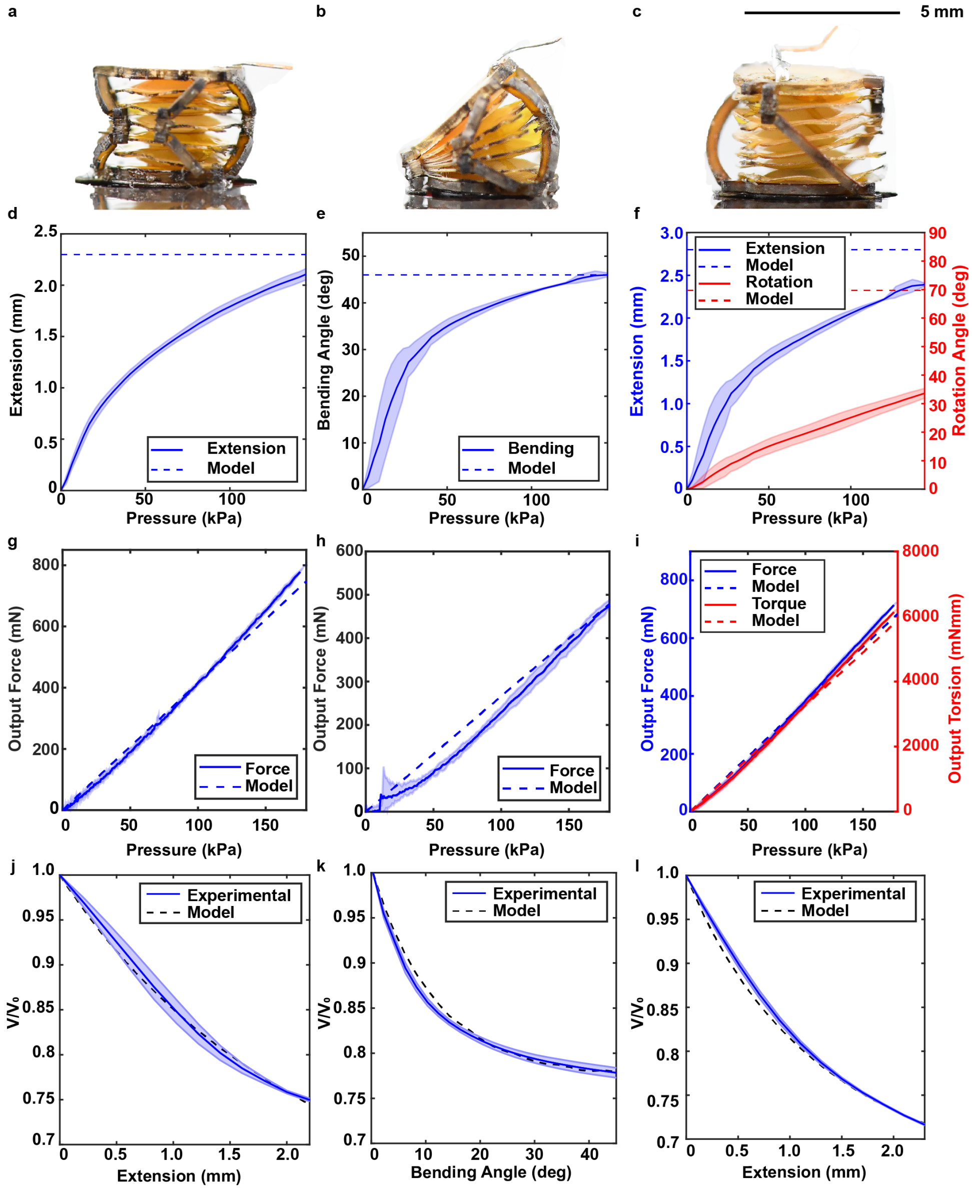

Fig. 2 Characterization of scaled-down SHY robotic modules. Images of expanded 5 mm OD (a) translational, (b) bending, and (c) roto-translational modules. Experimental results of range of motion of 5 mm OD (d) translational, (e) bending, and (f) roto-translational modules, and corresponding geometric calculation as shown in dashed lines. Output force performance of 5 mm OD (g) translational and (h) bending modules at a fully contracted state. (i) Output force and torque performance of 5 mm OD roto-translational modules at a fully contracted state. Measured normalized voltage (V/V_0) of (j) translational, (k) bending, and (l) roto-translational SHY robotic modules as each module actuates. The solid line is the mean resulting from three experiments, and the shaded area is the standard deviation. The dashed line is the output from the model.

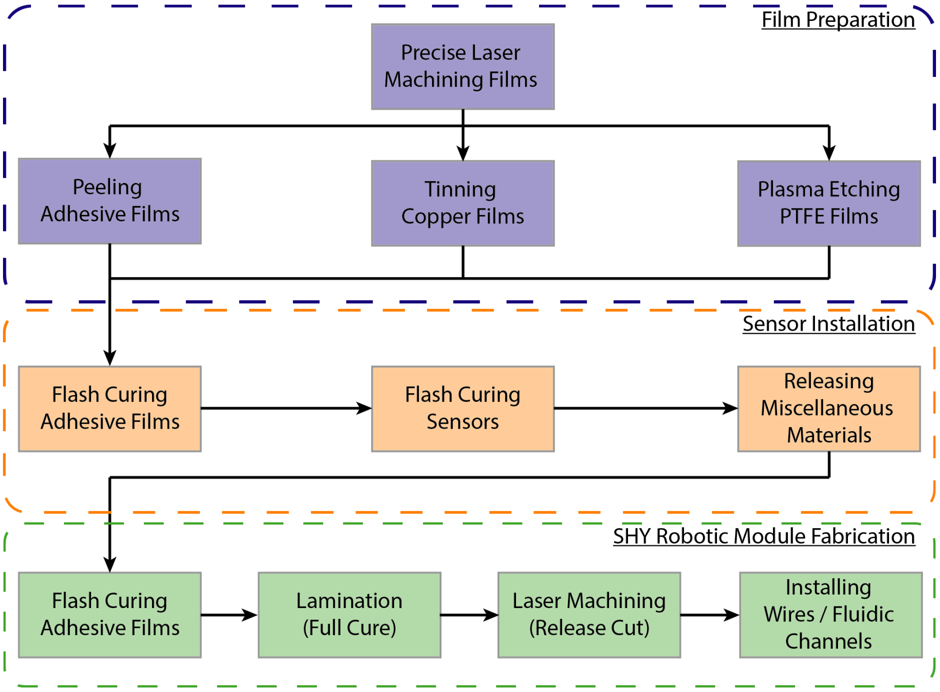

Fig. 3 Fabrication process flow chart. The fabrication process starts with film preparation, involving laser cutting of individual layers. Laser-processed adhesive films, copper films, and PTFE films are then post-processed (peeling, tinning, and plasma etching) in parallel. Next, electrodes for the ionic resistive sensor are installed on rigid layers. Post-processed layers are then laminated and subjected to laser machining once more to produce a SHY robotic module. To enable the functionality of the SHY robotic module, wires for sensing and a fluidic channel for actuation are installed.

Probing Liquid	Surface Tension, γ (mN/m)	Contact Angle (°)		
		Pristine	1 hour	1 week
Deionized Water	72.8	117.88	83.36	88.63
Glycerol	63.4	104.96	83.23	86.48
Ethylene Glycol	48	99.84	38.96	39.98
Chlorobenzene	33.6	37.86	20.6	21.72
Isopropanol	23	32.54	7.95	9.83

Table 1 Contact Angle Measurement on pristine and H_2 plasma etched PTFE films. Contact angles were measured using probing liquids with various surface tensions, including deionized water, glycerol, ethylene glycol, chlorobenzene, and isopropanol. Each reported contact angle measurement is the average of the left and right sides of the contact angle.

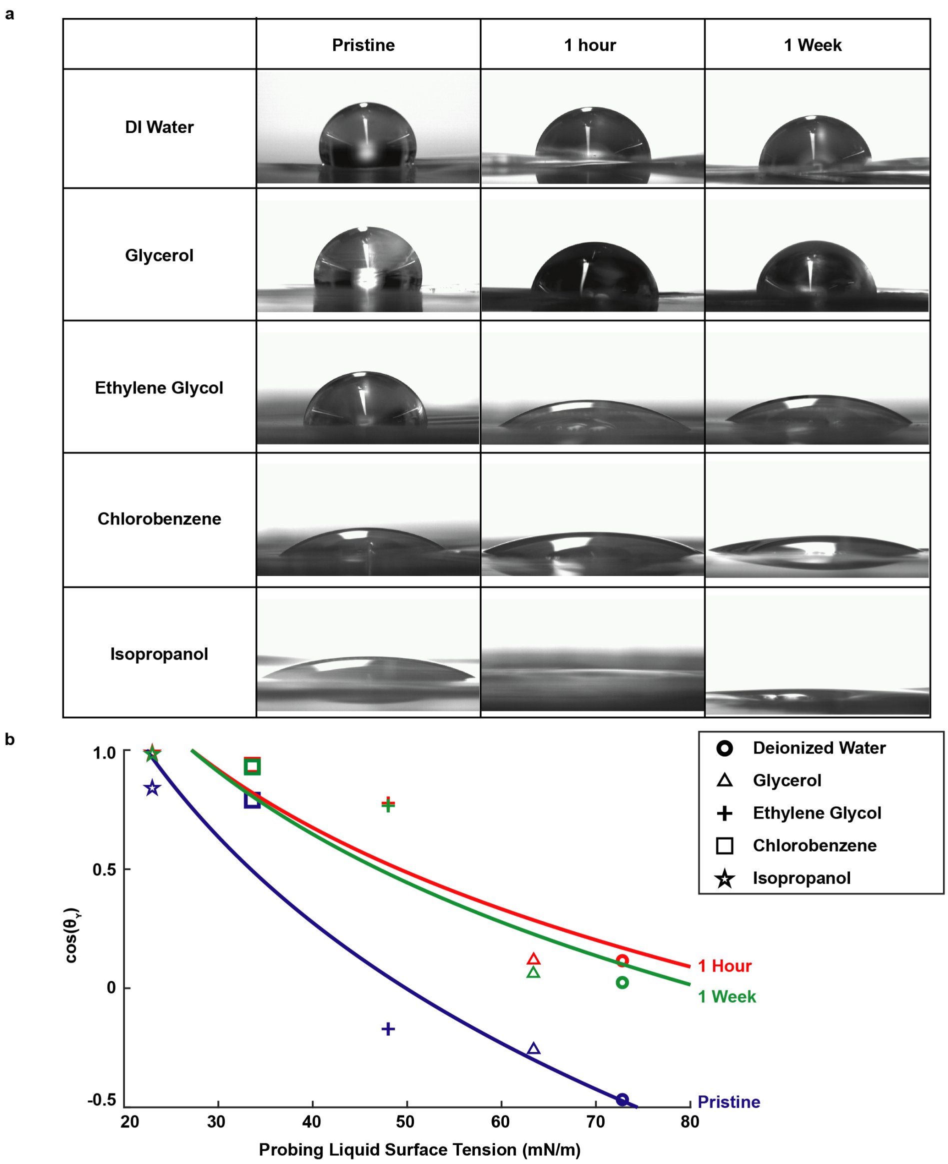

Fig. 4 Effects of H_2 Plasma Etching on PTFE Film Contact Angle Measurement. (a) PTFE films plasma-etched at two different time points (1 hour and 1 week after) were used to demonstrate permanent chemical modification. 12 μl of probing liquids including deionized water, glycerol, ethylene glycol, chlorobenzene, and isopropanol were dropped on the film to quantify the wettability of the films. (b) The Zisman plot of the pristine and plasma-etched films. γ_c represents the critical surface tension. The blue line represents the contact angle measurements of the pristine film. The red and the green lines represent the contact angle measurements of the film respectively after one hour and one week from H_2 plasma treatment.

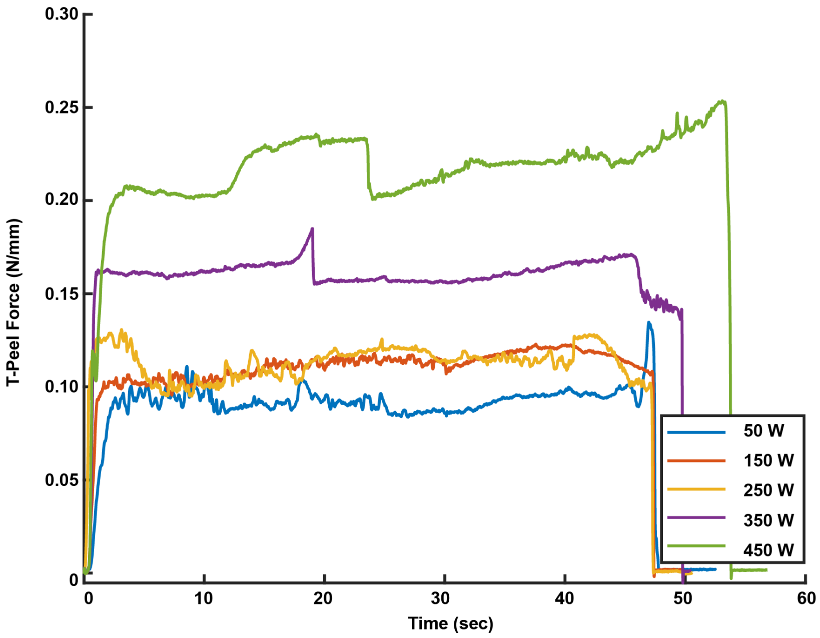

Fig. 5 T-peel test results. DuPont™ FR1500 adhesive peeling strength on H_2 plasma treated PTFE films was tested. The etching powers (50, 150, 250, 350, and 450 W) were varied to observe the effect of etching power on adhesive peeling strength.

Sample	Raw Peel Force (N)	T-Peel Force (N/mm)
50 W, 5 min	2.325	0.093
150 W, 5 min	2.676	0.107
250 W, 5 min	2.823	0.113
350 W, 5 min	4.044	0.162
450 W, 5 min	5.495	0.220

Table 2 Power varying T-peel test parameters. The effect of etching power was tested by varying it from 50 to 450 W. The bottom and top 10 % of data were removed from the average peel force calculation. The 450 W, 5 min etching recipe resulted in the highest T-peel force (0.220 N/mm).

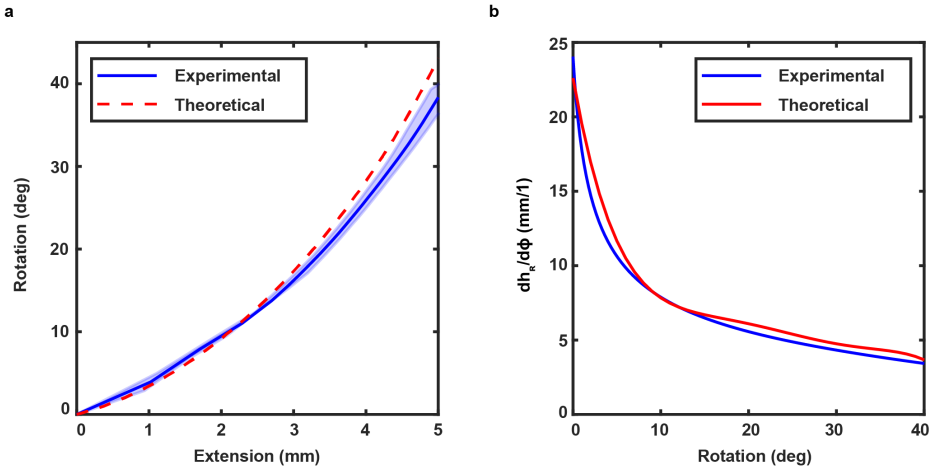

Fig. 6 Roto-translational module kinematics. (a) Range of motion (b) Kinematic coefficient based on experimental results and geometric modeling. The solid line is the mean resulting from three experiments on three prototypes, and the shaded area is the standard deviation. The dashed line is the output from the geometric model.

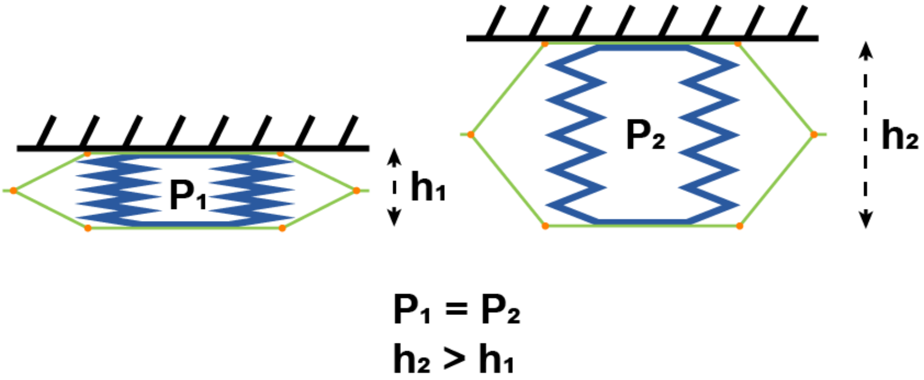

Fig. 7 Actuators at different expansion states. The output force of the actuator can vary depending on the position of external constraints, given the same internal pressure applied.

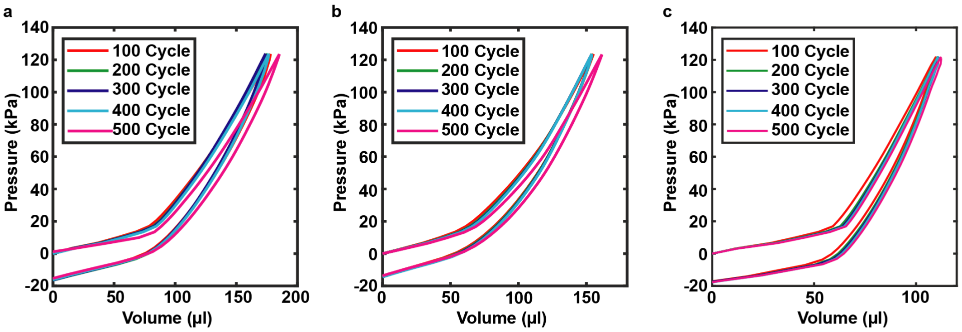

Fig. 8 Fatigue tests. Each actuator was actuated 500 times. The average pressure-volume data at every 100 cycles is shown in the figure. The figure shows pressure-volume (P - ∀) curves for (a) translational, (b) bending, and (c) Roto-translational SHY robotic module.

Authors	Fabrication Method	Fabrication Time *	Batch Fabrication	Manual Assembly	Actuation Method	Sensor Type	DOF	Size	Speed	Output Force / Torque
Our work	Plasma Etching, Lamination (heat and pressure)	-	Yes	No	Hydraulic	Resistive	4	5∼11.5 mm	4.48 mm/s 2.8 rad/s 4.14 mm/s	4.44 N 3.36 N 3.78 N, 84.89 Nmm
Russo et al. [12]	Soft Lithography, Lamination (pressure)	-	Yes	No	Hydraulic	Capacitive	1	1.25∼5 x 10∼20 mm	0.145∼ 2.09 rad/s	0.27∼ 10.68 Nmm
Rogantisky et al. [11]	Lamination (heat and pressure)	+	No	Yes	Pneumatic	X	2	15 mm	223 mm/s, 1.72 rad/s	4.87 N
Van Lewen et al. [14]	Lamination (heat and pressure)	+	No	Yes	Pneumatic	X	1	3 mm	0.42 mm/s	1.1 N
Niiyama et al. [10]	Lamination (heat and pressure)	+	Yes	No	Pneumatic	X	1	75x25 mm	N/A	100 N, 200 Nmm
Luo et al. [8]	Lamination (pressure)	+	No	Yes	Pneumatic	X	3	20x60 mm	N/A	N/A
Li et al. [6]	Lamination (heat and pressure)	+	No	Yes	Pneumatic	X	3	120x60 mm	N/A	N/A
Yang et al. [16]	Lamination (heat and pressure)	+	No	Yes	Pneumatic	Optical	1	60 mm	N/A	33 N

*: The fabrication time was estimated based on the given information.
-: Takes more than 2 hrs to fabricate
+: Takes less than 2 hrs to fabricate

Table 3 Performance comparison between our SHY fabrication method and similar ones based on a layer-by-layer approach for soft actuators and sensors for soft robots.

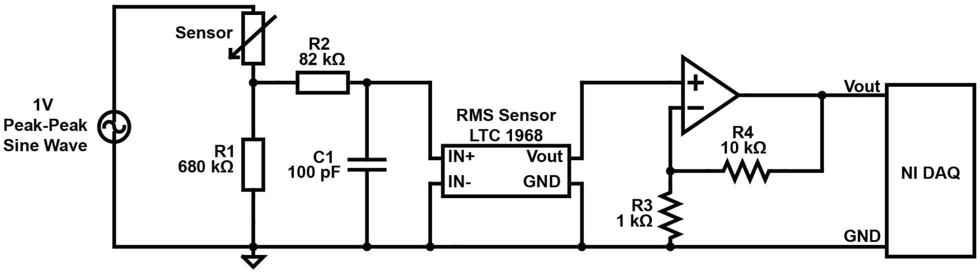

Fig. 9 Voltage divider circuit. 1V peak to peak with 10 kHz frequency sine wave is inputted to the circuit. The voltage drop across the shunt resistor is captured by the RMS sensor. A non-inverting op-amp is installed to amplify the output signal and accurately measure voltage using a NI-DAQ.

	Range (mm,°,°)	Sensitivity (1/mm, 1/°)	Max Standard Deviation
Translational Module	0 to 2.5	0.083	0.0068
	2.5 to 5	0.0296	
Bending Module	0 to 25	0.0068	0.0178
	25 to 50	0.0023	
Roto-translational Module	0 to 2.5	0.083	0.0219
	2.5 to 5.2	0.027	

Table 4 Sensor performance. Each sensor provides a non-linear, monotonic response. From these non-linear responses, the sensitivity of each module is computed by dividing the range into two linear regions. The max standard deviation of the sensitivity is computed for the entire range.

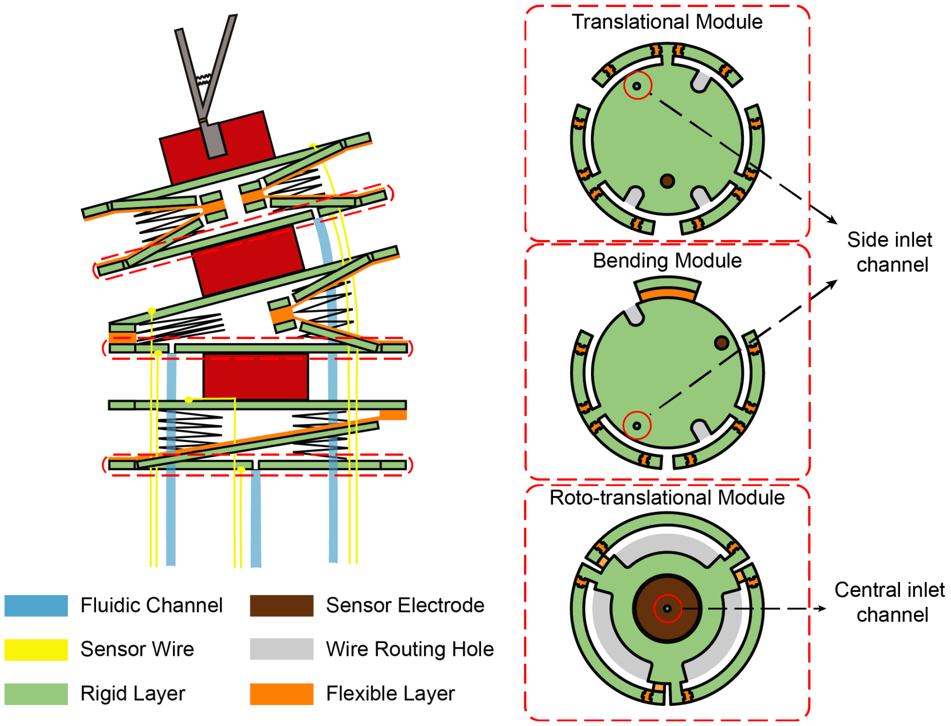

Fig. 10 SHY Continuum Robot. The illustrated SHY continuum robot is constructed (starting from the base of the robot to the end effector) with a roto-translational, a bending, and a translational module (i.e., R-B-T configuration). The translational and bending modules are designed with a side-inlet channel, and their fluidic channels are routed through wire routing holes.

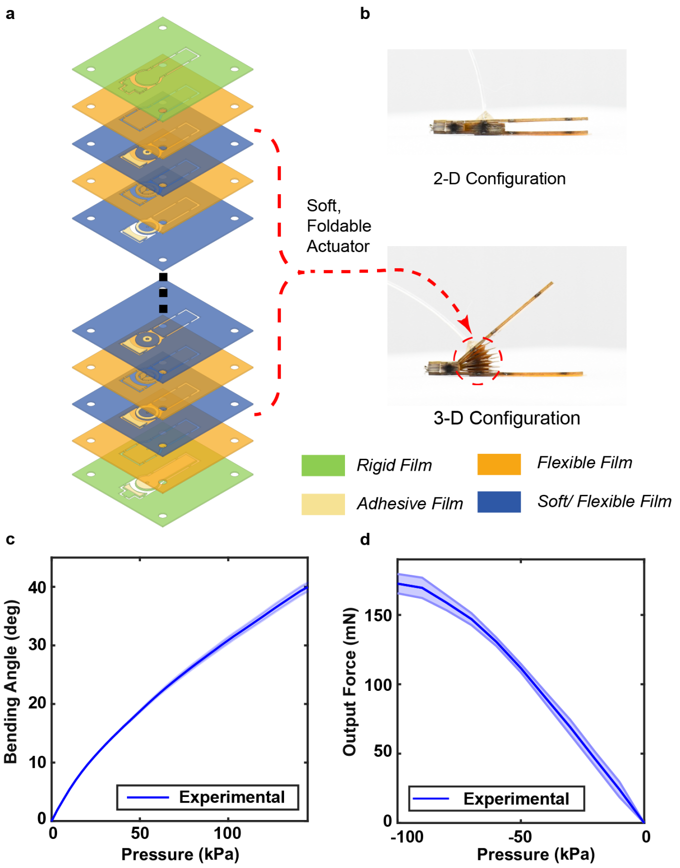

Fig. 11 SHY Robotic Grasper. The illustrated SHY robotic grasper is constructed using the same layer-by-layer manufacturing technique. (a) The SHY robotic grasper is manufactured out of rigid, flexible, soft and flexible, and adhesive films. (b) The SHY robotic grasper uses an embedded soft-foldable actuator to open and close its jaws. (c) The jaws can open up 40° by pressurizing the embedded soft-foldable actuator up to 150 kPa. The manipulation resolution of the grasper varies with the operating pressure range (0-150 kPa): 48°/kPa (0-20 kPa) and 0.23°/kPa (20-150 kPa). (d) The SHY robotic grasper can exert up to a maximum 180 mN of force at a pressure of -100 kpa.

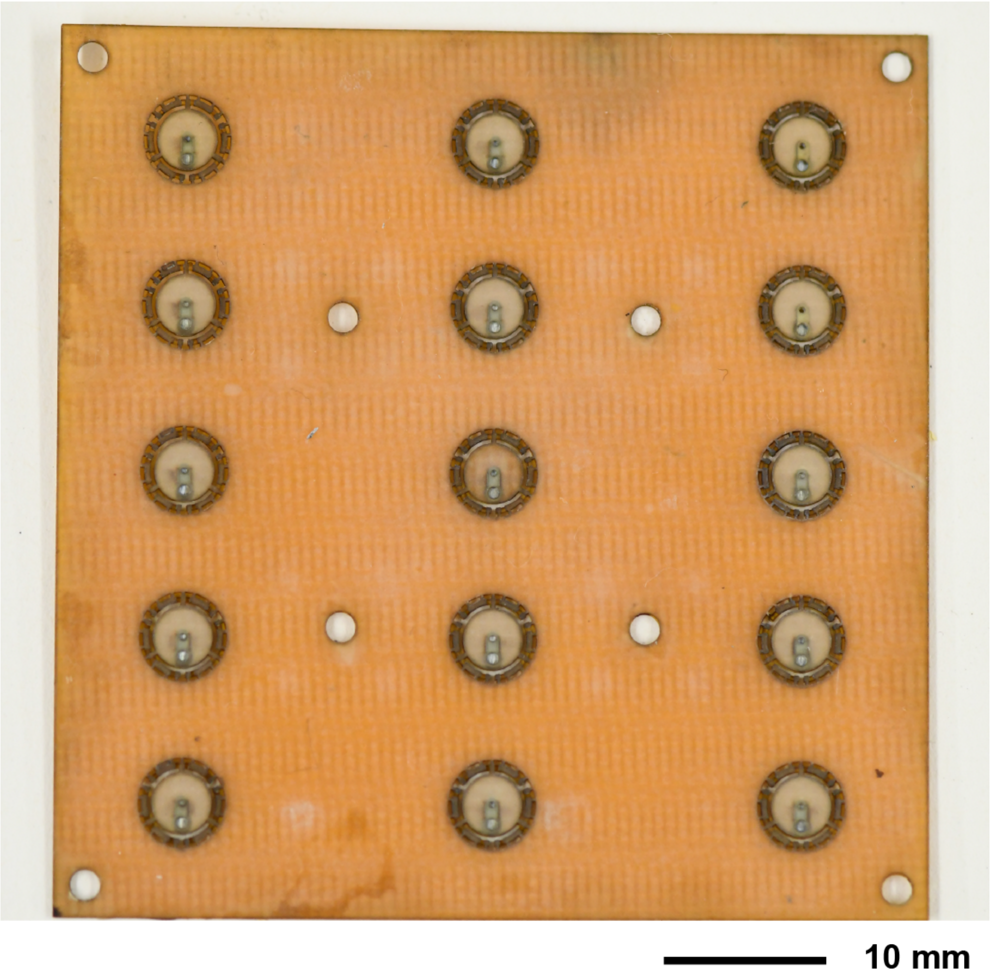

Fig. 12 SHY Robotic Module Batch Fabrication. We fabricated a total of 15 scaled-down (i.e., 5 mm OD) SHY robotic modules in a single batch in a square laminate of 5×5 cm. The diode-pumped solid-state (DPSS) ultraviolet (UV) laser precision micromachining system (Coherent Matrix 355 nm, 5 W) has a working area of 15×15 cm. Therefore, up to ≈105 scaled-down SHY robotic modules can be manufactured in a single batch, if desired.

Supplementary References

[1] Kang, E.T., Zhang, Y.: Surface modification of fluoropolymers via molecular design. Advanced Materials **12**(20), 1481–1494 (2000)

[2] Yang, H.D., Asbeck, A.T.: Design and characterization of a modular hybrid continuum robotic manipulator. IEEE/ASME Transactions on Mechatronics **25**, 2812–2823 (2020)

[3] Golahmadi, A.K., Khan, D.Z., Mylonas, G.P., Marcus, H.J.: Tool-tissue forces in surgery: A systematic review. Annals of Medicine and Surgery **65**, 102268 (2021)

[4] Inagaki, N., Tasaka, S., Narushima, K., Teranishi, K.: Surface modification of poly (tetrafluoroethylene) with pulsed hydrogen plasma. Journal of applied polymer science **83**(2), 340–348 (2002)

[5] Kim, S.R.: Surface modification of poly (tetrafluoroethylene) film by chemical etching, plasma, and ion beam treatments. Journal of applied polymer science **77**(9), 1913–1920 (2000)

[6] Li, S., Vogt, D.M., Rus, D., Wood, R.J.: Fluid-driven origami-inspired artificial muscles. Proceedings of the National academy of Sciences **114**(50), 13132–13137 (2017)

[7] Liu, C., Arnell, R., Gibbons, A., Green, S., Ren, L., Tong, J.: Surface modification of ptfe by plasma treatment. Surface engineering **16**(3), 215–217 (2000)

[8] Luo, Y., Zou, J., Gu, G.: Multimaterial pneumatic soft actuators and robots through a planar laser cutting and stacking approach. Advanced Intelligent Systems **3**(10), 2000257 (2021)

[9] Mosadegh, B., Polygerinos, P., Keplinger, C., Wennstedt, S., Shepherd, R.F., Gupta, U., Shim, J., Bertoldi, K., Walsh, C.J., Whitesides, G.M.: Pneumatic networks for soft robotics that actuate rapidly. Advanced functional materials **24**(15), 2163–2170 (2014)

[10] Niiyama, R., Sun, X., Sung, C., An, B., Rus, D., Kim, S.: Pouch motors: Printable soft actuators integrated with computational design. Soft Robotics **2**(2), 59–70 (2015)

[11] Rogatinsky, J., Gomatam, K., Lim, Z.H., Lee, M., Kinnicutt, L., Duriez, C., Thomson, P., McDonald, K., Ranzani, T.: A collapsible soft actuator facilitates performance in constrained environments. Advanced Intelligent Systems **4**(10), 2200085 (2022)

[12] Russo, S., Ranzani, T., Walsh, C.J., Wood, R.J.: An additive millimeter-scale fabrication method for soft biocompatible actuators and sensors. Advanced Materials

Technologies **2**(10), 1700135 (2017)

[13] Tolley, M.T., Felton, S.M., Miyashita, S., Aukes, D., Rus, D., Wood, R.J.: Self-folding origami: shape memory composites activated by uniform heating. Smart Materials and Structures **23**(9), 094006 (2014)

[14] Van Lewen, D., Janke, T., Lee, H., Austin, R., Billatos, E., Russo, S.: A millimeter-scale soft robot for tissue biopsy procedures. Advanced Intelligent Systems **5**(5), 2200326 (2023)

[15] Vesel, A., Lojen, D., Zaplotnik, R., Primc, G., Mozetič, M., Ekar, J., Kovač, J., Gorjanc, M., Kurečič, M., Stana-Kleinschek, K.: Defluorination of polytetrafluoroethylene surface by hydrogen plasma. Polymers **12**(12), 2855 (2020)

[16] Yang, H.D., Greczek, B.T., Asbeck, A.T.: Modeling and analysis of a high-displacement pneumatic artificial muscle with integrated sensing. Frontiers in Robotics and AI **5**, 136 (2019)

[17] Zhang, H., Paik, J.: Lattice-and-plate model: Mechanics modeling of physical origami robots. Soft Robotics **10**(1), 149–158 (2023)